Available online at www.sciencedirect.com
SCIENCE DIRECT®
International Journal of Heat and Fluid Flow 27 (2006) 1–20
International Journal of HEAT AND FLUID FLOW
www.elsevier.com/locate/ijhff

Detached eddy simulation of turbulent flow and heat transfer in a two-pass internal cooling duct

Aroon K. Viswanathan, Danesh K. Tafti *

Mechanical Engineering Department, Virginia Tech, 114 Randolph Hall, Blacksburg, VA 24061, United States

Received 10 January 2005; received in revised form 16 June 2005; accepted 14 July 2005
Available online 19 September 2005

Abstract

Numerical predictions of a hydrodynamic and thermally developed turbulent flow are presented for a stationary duct with square ribs aligned normal to the main flow direction. The rib height to channel hydraulic diameter (e/D_h) is 0.1, the rib pitch to rib height (P/e) is 10 and the calculations have been carried out for a bulk Reynolds number of 20,000. The capability of the detached eddy simulation (DES) version of the 1988 k–ω model has been validated in predicting the turbulent flow field and the heat transfer in a complete two pass channel. Results of mean flow quantities, secondary flows, friction and heat transfer are compared to experiments and large-eddy simulations (LES). It is concluded that in spite of shortcomings in predicting transition correctly at the entrance to the duct, DES surpasses the base capability of the underlying RANS model and predicts flow and heat transfer with good accuracy in a flow which is dominated by separation and reattachment of shear layers, unsteady vortex induced secondary motions, and strong streamline curvature. In all aspects it reproduces the correct physics and shows good quantitative comparisons with LES and experiments while reducing the computational complexity by nearly an order of magnitude.

Keywords: Detached eddy simulations (DES); Ribbed ducts; Turbine blade internal cooling

1. Introduction

Improved cooling methods for high temperature gas turbine components have been studied for the past couple of decades. The main emphasis for designers is to reduce the bulk temperatures of the components to increase their durability. So techniques such as film cooling and internal cooling are employed to cool the blades and the nozzles. Internal cooling involves forced-convection inside the blades by means of serpentine flow passages. Since convection can be increased by inducing turbulence in the flow, the boundary layer is tripped using various kinds of turbulators (ribs). This increases the heat transfer in the passages, but also results in an increase in friction in the duct. The flow and heat transfer in a ribbed internal cooling duct is a function of the flow Reynolds number and the geometric parameters such as the rib height to hydraulic diameter ratio, the rib pitch, the aspect ratio of the duct, the angle of the rib with respect to the flow and the shape of the rib as shown by some studies (Johnson et al., 1994).

The present work is motivated by the need to accurately predict the heat transfer in such flows. The flow behind a rib though geometrically simple, has some complex features: separation of the boundary layer, a curved shear layer, primary and secondary recirculation, reattachment of the boundary layer, recovery, etc. Additionally the reattachment is followed by redevelopment of the downstream boundary layer. These complex features of the flow pose a big challenge in the numerical prediction of the flow behind the rib. Numerical techniques range from resolving the full flow field, such as in direct numerical simulations (DNS), to the modeling of all turbulent scales using Reynolds averaged Navier–Stokes equations (RANS). Though inexpensive, RANS models are not reliable especially for flows with massive separation. Studies show that the turbulent

* Corresponding author. Tel.: +1 540 231 9975; fax: +1 540 231 9100.
E-mail address: dtafti@vt.edu (D.K. Tafti).

0142-727X/$ - see front matter © 2005 Elsevier Inc. All rights reserved.
doi:10.1016/j.ijheatfluidflow.2005.07.002

Nomenclature

C_f	skin-friction coefficient
D_h	hydraulic diameter (characteristic length)
e	rib height
f	Fanning friction factor
k	thermal conductivity
Nu	local Nusselt number $[Nu = 1/(\theta_s - \theta_{ref})]$
$\langle Nu \rangle$	spatially averaged Nusselt number $\left[\langle Nu \rangle = \left(\int_A \int \frac{1}{\theta_s - \theta_{ref}} dA\right) \Big/ \left(\int_A \int dA\right)\right]$
$\vec{n}$	surface normal vector
P	total pressure OR rib pitch
p	fluctuating or homogenized pressure
q''	constant heat flux on duct walls and rib
Re	Reynolds number based on bulk velocity
$\vec{u}$	Cartesian velocity vector
W	width of the 180° bend $= 0.5D_h$
$\vec{x}$	physical coordinates
β	mean pressure gradient
ε_{ijk}	Permutation tensor
γ	mean temperature gradient
θ	non-dimensional temperature $[\theta = (T - T_{in})/(q'' D_h/k)]$
θ_{ref}	non-dimensional reference temperature $\left[\theta_{ref} = \left(\int_{A_x} \int |u\theta| \cdot dA_x\right) \Big/ \left(\int_{A_x} \int |u| \cdot dA_x\right)\right]$
ξ	computational coordinates

Subscripts

b	bulk
o	smooth duct
s	surface
t	turbulent parameters

viscosity and the turbulent shear stress are usually over-predicted by the two equation models in such flows (Driver and Seegmiller, 1985; Amano and Goel, 1995). This results in the rapid spreading of the shear layer due to which the reattachment is predicted early.

Most of the reported computational predictions in ribbed ducts are focused on the solution of the Reynolds averaged Navier–Stokes (RANS) equations. Different closure models have been used, and it has been observed that while eddy-viscosity models which assume isotropy of turbulence (Prakash and Zerkle, 1995) fail to capture the flow accurately, more complicated models have performed reasonably well (Jia et al., 2002).

Liou et al. (1992) used a k–ε algebraic stress model to predict flow in a stationary 2D ribbed duct with ribs on one wall. Their studies showed that the k–ε model failed to predict the flow accurately while the k–ε–A model, which accounts for the anisotropy of turbulence, gave reasonable results. Saidi and Sunden (2001) also used k–ε models in a periodic channel with inline orthogonal ribs, and the computations showed mixed results. Iacovides (1998) carried out computations using k–ε and low-Re zonal differential stress models (DSM) in a periodic ribbed duct for stationary and rotating cases. Though a reasonable flow behavior was predicted by the k–ε model, the thermal behavior was not predicted accurately. The low-Re DSM model gave better predictions than the k–ε model. Iacovides and Raisee (1999) introduced a modified version of the Yap correction to the low-Re DSM models and obtained reasonable heat transfer results in a 180° bend channel. Ooi et al. (2002) present predictions using a v^2–f model on orthogonal inline ribs and found that the model performs better than the k–ε and S–A RANS models.

Rigby (1998) studied the heat and mass transfer in a two pass ribbed channel with a 180° turn using a modified version of Menter's SST model (Menter, 1992, 1993). Both stationary and rotating cases were studied. Low Reynolds number flows were considered (5200–7900) and it was observed that the standard turbulence models failed to predict the reattachment accurately. So modifications in the ω boundary conditions were required for the model to predict the flow attachment accurately.

Large eddy simulations (LES) have been used in the past to study the heat transfer in ribbed channels. Murata and Mochizuki (2001) studied the effect of Coriolis force and the duct cross-section on the heat transfer in smooth and ribbed channels. Watanabe and Takahashi (2002) carried out LES computations and experimental studies in a rectangular channel with traverse ribs which are heated from one side and obtained good agreement with the experiments. The studies also revealed the unsteady mechanism that enhanced the heat transfer in the ribbed channel. Tafti (2005) used 96^3 and 128^3 grids to predict the fully developed flow and heat transfer in a channel with orthogonal ribs. The computations also gave a comprehensive knowledge of the major flow structures in the flow field and compared very well with experiments.

LES computations on the developing region of an internal cooling duct were carried out by Sewall et al. (accepted for publication). The total number of grid points required for a nine ribbed developing case was around 8.85×10^6. The flow and the heat transfer were observed to be near fully developed by the fourth rib. The flow features and the heat transfer after the 5th rib showed good agreement with the fully developed profiles. Sewall et al. (accepted for publication) used LES to compute the flow and heat transfer in a 180° bend with three ribs upstream and downstream of the bend. A total of 8.4×10^6 cells were used for the computation. The flow and heat transfer predicted showed good agreement with the experimental data.

While accurate results have been obtained with the LES computations, the grid requirements are very demanding and the LES computation of a complete multi-pass channel would be too expensive. The resolution in the boundary layer has to be fine and increases with Reynolds number. This calls for a special treatment of the boundary layer to limit the number of grid points. One of the several techniques available for wall modeling is detached eddy simulation (DES), which was proposed by Spalart et al. (1997). This technique, initially proposed based on the Spalart–Allmaras turbulence model, treats the inner layer in a RANS mode and by modifying the length scale in the destruction term the model switches to a sub-grid type formulation. Later this technique was generalized by Strelets (2001) who defined a DES scheme for the Menter's shear stress transport model. By this modified definition, DES acts more than a wall model by reducing the solution to a RANS computation in regions (even away from the wall) where the turbulent length scale is less than the grid length scale. In the recent past many calculations applied to external aerodynamic flows have been reported. These computations have accurately captured the flow physics over geometries as complicated as an airplane (Squires et al., 2002; Forsythe et al., 2002), car models (Kapadia et al., 2003), etc. DES computations on the fully developed flow and heat transfer in a channel with normal ribs were carried out by Viswanathan and Tafti (2004). These computations showed excellent agreement with the experiments and LES results and were an order of magnitude less expensive than LES.

2. Objective of the study

The objective of this work is to evaluate the capabilities of the DES version of the 1988 k–ω model in predicting the turbulent flow and heat transfer in a two-pass internal cooling ribbed duct with a 180° turn. This is a first such application of DES to internal flow and heat transfer and builds on previous work (Viswanathan and Tafti, 2004) which applied DES to fully developed flow and heat transfer in the same ribbed geometry. The present results are compared with LES calculations (Sewall et al., accepted for publication; Sewall and Tafti, 2005) and experiments (Rau et al., 1988; Han et al., 1988). Of particular interest is the ability of DES to predict flow transition, including flow development in the duct, flow in the 180° bend and the development of secondary flows in the duct cross-section. The overall motivation is to evaluate the use of DES in lieu of LES for the accurate prediction of heat transfer in ribbed internal cooling ducts.

3. Computational model and the governing equations

Computations are carried out for a ribbed square channel with a rib pitch to rib height (P/e) of 10 and rib height to hydraulic diameter (e/D_h) of 0.1 for a bulk Reynolds number of 20,000. The ribs are placed normal to the flow direction and have a square cross-section. Since DES is less expensive than LES, a complete analysis of a two-pass channel with 12 sets of ribs in the first and the second pass has been carried out. The two passes are connected by a 180° bend whose width (W) is half the hydraulic diameter ($W/D_h = 0.5$). Around 262,000 cells are used in each rib section with a total of around 7.7×10^6 cells to discretize the whole channel with the 180° bend. The walls (ribbed and side walls) and the ribs are heated by a constant heat flux (q'') and a stationary case is considered. The governing flow and energy equations are non-dimensionalized by a characteristic length scale which is chosen to be the hydraulic diameter of the channel (D_h), a characteristic velocity scale given by the inlet velocity (U_0), and a characteristic temperature scale given by $q'' D_h/k$.

Therefore the non-dimensional time dependent Navier–Stokes and energy equations in transformed coordinates are

Continuity

$$\frac{\partial}{\partial \xi_j}\left(\sqrt{g}U^j\right) = 0,$$

Momentum

$$\frac{\partial}{\partial t}\left(\sqrt{g}u_i\right) + \frac{\partial}{\partial \xi_j}\left(\sqrt{g}U^j u_i\right) = -\frac{\partial}{\partial \xi_j}\left(\sqrt{g}(\vec{a}^j)_i p\right) + \frac{\partial}{\partial \xi_j}\left(\left(\frac{1}{Re} + \frac{1}{Re_t}\right)\sqrt{g}g^{jk}\frac{\partial u_i}{\partial \xi_k}\right),$$

Energy

$$\frac{\partial}{\partial t}\left(\sqrt{g}\theta\right) + \frac{\partial}{\partial \xi_j}\left(\sqrt{g}U^j\theta\right) = \frac{\partial}{\partial \xi_j}\left(\left(\frac{1}{PrRe} + \frac{1}{Pr_t Re_t}\right)\sqrt{g}g^{jk}\frac{\partial \theta}{\partial \xi_k}\right),$$

where $\vec{a}^i$ are the contravariant basis vectors,[1] $\sqrt{g}$ is the Jacobian of the transformation, g^{ij} are the elements of the contravariant metric tensor, $\sqrt{g}U^j = \sqrt{g}(\vec{a}^j)_i u_i$ is the contravariant flux vector, u_i is the Cartesian velocity vector, and θ is the temperature. The turbulence closure terms in the momentum and the energy equations are evaluated using the 1988 k–ω RANS model (Wilcox, 1988).

4. Detached eddy simulations

Reynolds averaged Navier–Stokes (RANS) models have been used for a long time to solve complex flows. These models demand reasonable computational power, but the solution obtained is not very reliable and repeatable, particularly in complex anisotropic flows with secondary strain rates. Direct and large eddy simulations resolve the unsteady turbulent eddies and give a solution that mimics

[1] The notation $(\vec{a}^j)_i$ is used to denote the ith component of vector $\vec{a}^j$. $(\vec{a}^j)_i = \partial \xi_j / \partial x_i$.

the exact flow-field. The typical spatial resolution in LES is much less than that mandated by the Kolmogorov length scale, and eddies with scales larger than this length scale are directly resolved. However, the near wall resolution in LES increases with Reynolds number, making the technique expensive for high Reynolds number flows.

DES is a modification of a RANS model in which the model switches to a subgrid scale formulation in regions fine enough for LES calculations (Spalart et al., 1997). It is a non-zonal approach and provides a single smooth velocity field across the RANS and the LES regions of the solution. Though DES was initially formulated for the Spalart–Allmaras model, it can be implemented with other RANS models (Strelets, 2001), by appropriately modifying the length scale which is explicitly or implicitly involved in the RANS model. Regions near solid boundaries and where the turbulent length scale is less than the maximum grid dimension are assigned the RANS mode of solution. When the turbulent length scale exceeds the grid dimension, the regions are solved using the LES mode. Therefore, the grid resolution is not as demanding as pure LES, considerably reducing the cost of the computation.

A DES formulation is implemented in the k–ω equations (Wilcox, 1988) by writing the dissipation term in the k-equation in terms of a representive turbulent length scale, i.e., $D^k = \beta^* k\omega = k^{3/2}/\delta$ where δ is found as the minimum of the turbulent length scale $l_{k-\omega} = \sqrt{k}/\beta^*\omega$ and a grid length scale $C_{\mathrm{DES}}\Delta$ as $\delta = \min(l_{k-\omega}, C_{\mathrm{DES}}\Delta)$. When $C_{\mathrm{DES}}\Delta < l_{k-\omega}$, the model switches to a Smagorinsky type sub-grid scale model. Here Δ is calculated as the maximum directional grid spacing ($\Delta = \max(\Delta_x, \Delta_y, \Delta_z)$). A DES constant $C_{\mathrm{DES}} = 0.61$ is used (Strelets, 2001).

5. Numerical method

The governing equations for momentum and energy are discretized with a conservative finite-volume formulation using a non-staggered grid topology. The Cartesian velocities, pressure, and temperature are calculated and stored at the cell center, whereas contravariant fluxes are stored and calculated at the cell faces. For the time integration of the discretized continuity and momentum equations, a projection method is used. The temporal advancement is performed in two steps, a predictor step, which calculates an intermediate velocity field, and a corrector step, which calculates the updated velocity at the new time step by satisfying discrete continuity. A second order central difference scheme is used to discretize the momentum and energy equations. The equations for the turbulent kinetic energy and the dissipation rate are also solved using a second order central difference scheme subject to a TVD limiter.

The computer program GenIDLEST (generalized incompressible direct and large eddy simulations of turbulence) used for these simulations has been applied extensively to study air-side heat transfer augmentation in compact heat exchangers and internal cooling in gas turbines (Abdel-Wahab and Tafti, 2004a,b; Sewall and Tafti, 2004a,b; Viswanathan and Tafti, 2005; Viswanathan et al., 2005; Patrick and Tafti, 2004). Details about the algorithm, functionality, and capabilities can be found in Tafti (2001).

6. Computational details

Detached eddy simulations are carried out in a complete two-pass channel with 12 ribs in the first and the second passes, which are connected by a 180° bend. Each rib section (block) consists of two in-line ribs placed at the center of the channel at the top and the bottom. The grid and the coordinate system used are shown in Fig. 1. The grid in a rib pitch consists of 65 nodes in the streamwise direction, of which 13 nodes lie directly over the rib, with 53 nodes in the inter-rib space. In the cross-stream direction the grid consists of 65×65 nodes with 13 nodes each in the regions of the rib, covering the rib height of e and 41 nodes in the middle of the channel and 65 nodes distributed using a monotonic spline distribution along the span (Fig. 1). The grid distribution is symmetric in the y and the z directions. The grid generated for one pitch has been tested and found to be optimal for a DES computation (Viswanathan and Tafti, 2004).

In order to resolve the viscous sub-layer, a wall normal spacing of $\Delta^+ < 1$ is provided in regions close to the rib and the channel walls, with about 3–4 points in the region $\Delta^+ < 10$. The streamwise grid distribution gives $\Delta^+ < 1$ near the ribs and $\Delta^+_{\max} \sim 100$ in the inter-rib space. The spanwise distribution is a monotonic spline distribution with $\Delta^+ < 1$ near the side walls and $\Delta^+_{\max} \sim 30$ at the center. The grid spacing in the x, y, z directions, for a rib pitch, are shown in Fig. 1(b). This distribution allows a major part of the boundary layer to be treated in the RANS mode. In total, each unit was discretized into $64 \times 64 \times 64$ cells and was divided into four equal blocks in the spanwise direction to facilitate parallel processing. The 180° bend was discretized into $64 \times 64 \times 32$ cells and divided into two blocks. The second leg of the duct had an outlet region, which was around 4 hydraulic diameters long. All these sum to 7.7×10^6 cells which are distributed in 110 blocks.

A non-dimensional time step (non-dimensionalized based on the bulk velocity and the hydraulic diameter of the duct) of 1×10^{-4} was used in all of the cases. Calculations are initiated by assuming a uniform flow velocity in the computational domain and imposing a uniform laminar flow inlet profile, approximating the flow exiting a plenum into the ribbed channel. Time evolution of bulk quantities such as surface-averaged Nusselt numbers and friction factors are monitored as the solution is allowed to reach a statistically steady state for about 20 non-dimensional time units. The mean characteristics of the flow are obtained by averaging the solution for an additional 20 time units.

The augmentation ratios for both heat transfer and friction are calculated with reference to a smooth channel. The reference values for Nusselt number and friction factor for

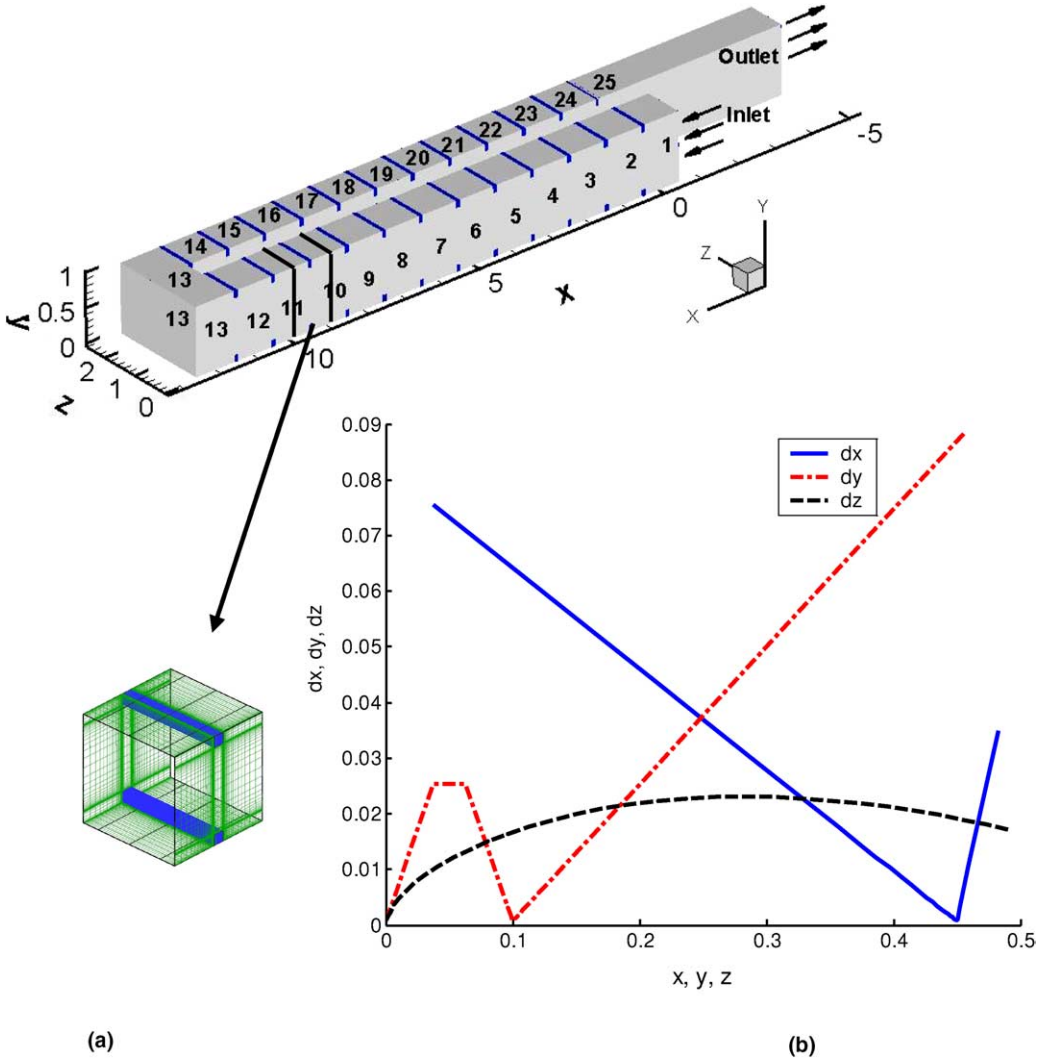

Fig. 1. (a) Schematic diagram representing the two pass channel used in the study and the grid in a unit rib section. The numbers 1–25 represent the blocks (section #) used for spatial averaging of friction factor and the heat transfer augmentation. (b) Variation of grid spacing in x, y, z directions for a quarter of the duct cross-section for half a rib pitch.

a smooth duct are obtained from the correlations (Incropera and Dewitt, 2002):

$$Nu_0 = 0.023 \cdot Re_b^{0.8} \cdot Pr^{0.4},$$

$$f_0 = 0.046 \cdot Re_b^{-0.2}.$$

7. Results and discussion

In the current study, DES is carried out in a complete two-pass channel with 12 ribs in the first and second passes, connected by a 180° bend. The flow in the first pass of the duct is compared with LES computations by Sewall and Tafti (2004a) and experiments by Rau et al. (1988). The flow in the 180° bend is compared with LES results in the bend by Sewall and Tafti (2005) and experimental results by Han et al. (1988) and Sewall et al. (accepted for publication). Germano's dynamic model was used for the LES computations and the computations did not employ any wall modeling. The transport properties are assumed to be temperature independent. Density variations are not considered and so buoyancy effects have been neglected. The LES computations have been validated extensively with experiments in Sewall et al. (accepted for publication), and except for some differences at the center of the duct and in the 180° bend, all physical phenomena characterized by mean and turbulent rms quantities are reproduced with excellent quantitative accuracy.

7.1. Mean flow field

7.1.1. LES Characteristics of the solution

Fig. 2 shows the RANS–LES regions in the solution. DES being a hybrid scheme solves certain regions of the flow field in a LES mode (DES = 1.0 in the figure) when the grid is fine enough and certain regions in RANS mode (DES = 0.0 in the figure) when the grid is coarse compared

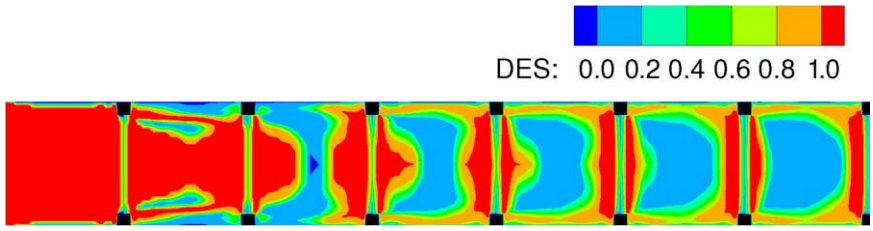

Fig. 2. DES regions in the center of the domain. A value of 0.0 represents a region completely solved in RANS mode while a value of 1.0 represents a complete LES mode.

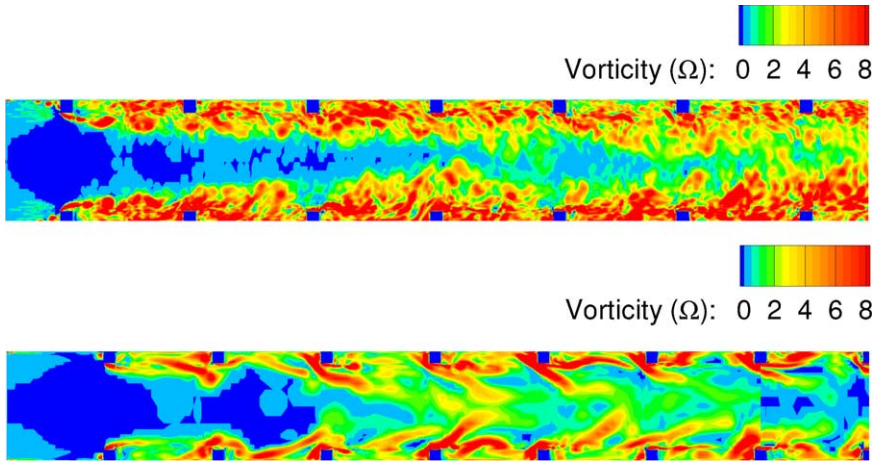

Fig. 3. Contours of coherent vorticity in the center of the duct as predicted by LES (top) and DES (bottom).

to the turbulence length scale. While in a Spalart–Allamaras DES model the turbulence length scale is determined by the distance from the wall, in the two equation models the turbulent length scale is derived from the solution of the k and ω equations, due to which the turbulent length scale is a time dependent variable. The temporal variation of the turbulent length scale accounts for the partially LES–partially RANS regions ($0.0 < \mathrm{DES} < 1.0$) in the computation. Thus in regions where the instantaneous turbulence length scale is smaller than the grid size the model acts as a URANS model, while in regions where the grid length scale is smaller than the instantaneous turbulent length scale the model switches to a sub-grid scale formulation.

At the laminar inlet, the flow is mostly resolved in the LES mode, which changes to a LES-RANS mode as the flow develops in the duct. Immediately downstream of the first rib, RANS regions develop in the vicinity of the separated shear layer and the resulting recirculating zone, whereas the center of the duct is still treated in LES mode. By the third rib most of the flow in the center of the duct is treated in RANS mode whereas a hybrid RANS-LES mode is used in the separated shear layer and the recirculating region downstream of each rib.

A comparison of the instantaneous coherent vorticity as predicted by LES and DES is shown in Fig. 3. It is observed that LES resolves scales much smaller than the DES computation. However, it is observed that the magnitude of coherent vorticity as predicted by DES is consistent with the magnitudes predicted by LES. The vorticity is low at the inlet before the flow is tripped by the first rib. Regions in the inter-rib space experience a lot of turbulence and consequently the vorticity magnitude in this region are large. This region of high turbulence propagates towards the center of the duct as the flow progresses downstream. These features predicted by LES are captured accurately by DES.

7.1.2. Streamwise flow development in first pass

Fig. 4 shows the development of the streamwise flow velocity. The LES calculation (Sewall et al., accepted for publication) shows that the separated shear layer at the first set of ribs immediately transitions to turbulence, which starts diffusing toward the duct wall and the centerline. The separation zone behind the first rib extends the whole pitch and reattaches just upstream of the second set of ribs. The first rib accelerates the bulk flow in the cross-section, and together with the large separated region, contributes to a significant pressure loss. However, at the second rib, because of the increased mixing promoted by turbulence, the separated zone extends only half the rib pitch, after which the flow structure quickly settles down to a near fully developed state,[2] with small changes occurring in the flow

[2] Although the flow quantities still change in magnitude further downstream, a "near-fully developed" state is established by the third to fourth rib.

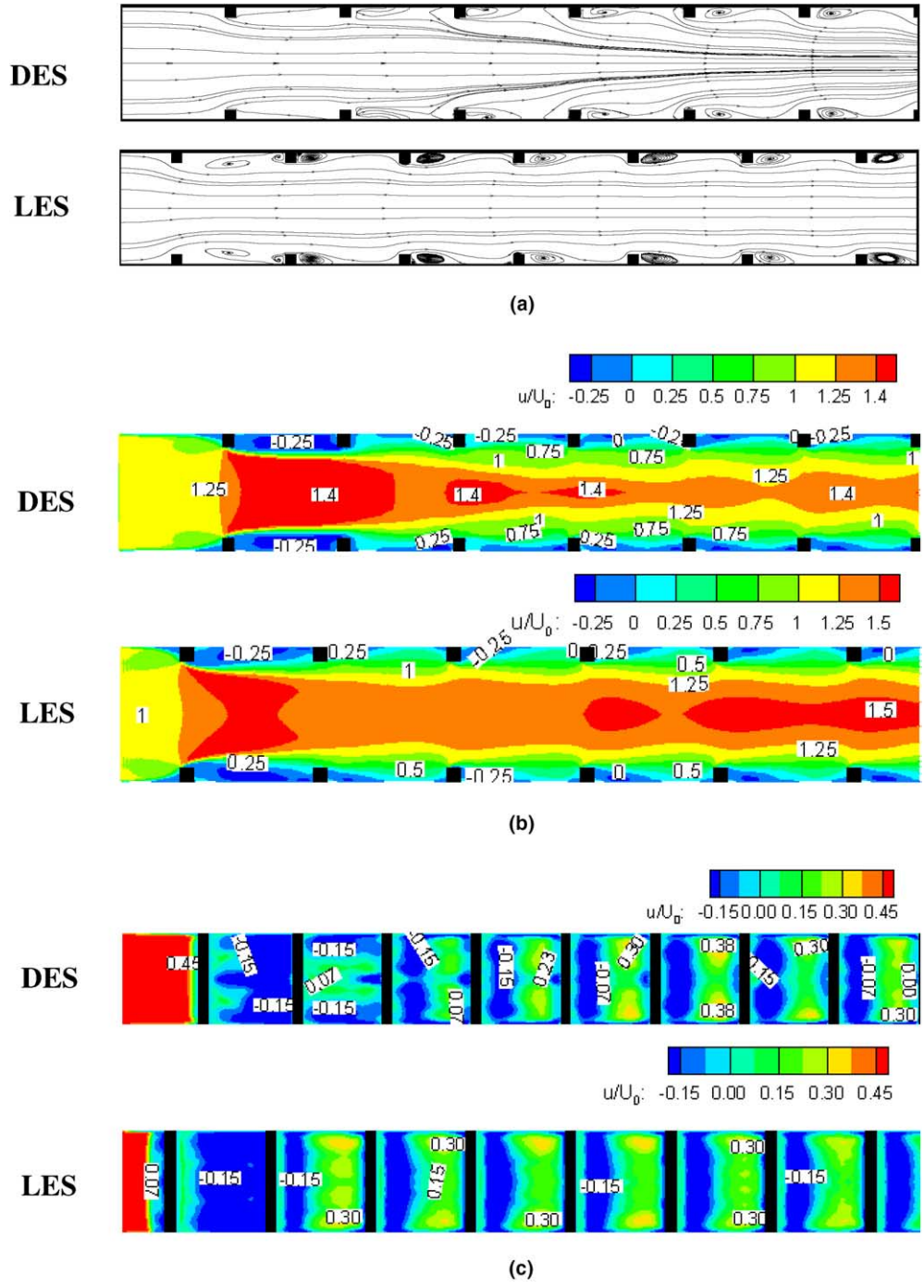

Fig. 4. (a) streamlines in the center plane of the developing region showing fully developed flow by the fifth rib. (b) Streamwise velocity at the center of the duct ($z = 0.0$). (c) Streamwise velocity at $y/e = 0.15$ showing the development of the flow.

structure and turbulent characteristics. This can be clearly identified in Fig. 4(a)–(c). The uniform streamwise velocity profile at the entrance to the duct quickly attains a flat turbulent flow profile in the duct.

The DES results are different than those predicted by LES for the first three to four rib pairs. At the first three ribs, the separation zones are much larger than in LES and the streamwise velocity distribution in the cross-section is less "plug-like", but shows a gradual increasing trend towards the center of the duct, both of which imply that DES is unable to predict the rapid transition to a turbulent state. This can be clearly observed in Fig. 3. While the DES calculation delays transition, URANS calculations with the same model show an immediate transition to a near fully developed state immediately after the first rib. So while the k–ω model in the URANS mode is capable of

predicting shear layer transition, albeit early with no spatial development, the DES calculation does not. Fig. 2 indicates that the region downstream of the first rib is mostly treated in LES mode. Since the grid used in the DES calculation is much coarser than the equivalent LES calculation, it could be probable that the LES on the coarse grid is not sufficiently well resolved to predict the transition accurately. While LES reaches a quasi-periodic state after the third rib, DES reaches a similar state after the fourth to fifth rib pair.

At a plane passing through $y/e = 0.15$, Rau et al. (1988) had earlier observed the maximum velocity to lie at a distance of around $0.15D_h$ from the wall in the fully developed region. A similar observation was made in the fully developed cases computed earlier using LES and DES (Viswanathan and Tafti, 2004). In the present calculation, the feature is observed initially between the 5th and the 6th ribs and in between the subsequent ribs, though slight differences in size are observed. On the other hand, with LES this feature appears as early as the second pair of ribs and is fully established by the third rib. The levels of velocity magnitudes ($u = 0.30$–0.38) also agree well with the fully developed cases studied (Viswanathan and Tafti, 2004; Tafti, 2005).

In spite of these differences between LES and DES at the early stages of flow development, the predictions using the two methods match well with each other and experiments after the fifth rib. The velocity profiles in the vicinity of rib 5 shows good agreement with the experiments (Rau et al., 1988) and the LES. Fig. 5 shows the streamwise velocities measured at a plane passing through the center at the $y/e = 0.1$ plane. Fig. 5(a) shows the development of the flow from the inlet to the 8th rib. It is observed that after the 5th rib the velocity profile predicted repeats itself showing signs of a fully developed flow. A comparison of the development of the flow at a plane passing through the rib ($y/e = 0.25$) shows that the DES results compare well with the LES results after 5 ribs from the inlet. DES slightly under-predicts the velocities in the recirculation zone in comparison to LES, but in general the predictions are in good agreement. Fig. 5(b) shows a more detailed comparison of flow acceleration in the inter-rib region at $y/e = 0.1$. The separated region behind the rib experiences a reverse flow, which is evident from the negative velocities behind the rib up to the reattachment region. The flow accelerates after reattachment and separates in front of the next rib as shown by the small negative velocities upstream of the rib ($x = 4.35$). The separation in front of the rib and the secondary recirculation trapped behind the rib are predicted accurately, and the velocity magnitudes are consistent with the fully developed experimental data and LES computations.

7.1.3. Development of secondary flows

Secondary flows in the duct cross-section have a large effect on heat transfer augmentation on the smooth walls. Unlike skewed or angled ribs, which exhibit strong secondary flow patterns, normal rib induced secondary flows are comparatively weak but highly localized and strong near the junction of the rib with the side walls. The vortex shedding at the junction induces strong spanwise velocities in the vicinity of the smooth wall. This feature is difficult to predict by standard eddy-viscosity RANS and URANS models (Ooi et al., 2002; Viswanathan and Tafti, 2004). Fig. 6 shows the development of the spanwise velocity contours at a plane near the side wall ($z/D_h = 0.05$). LES predicts the establishment of this feature by the third rib pair, whereas DES predicts it only after the fourth rib pair, however after it is established, the magnitudes are consistent between the two methods. The lateral w-velocities measured above the rib along a line close to the smooth side wall ($y/e = 1.5$, $z/D_h = 0.45$), also shows very good agreement of the secondary flow in the vicinity of rib 5 with the fully developed experimental results and LES computations. It is observed that there is little spanwise movement of the fluid in the region after reattachment while in the vicinity of the ribs ($x = 4.4$–4.6) a strong secondary velocity is observed. It is also noted that the same k–ω model when used in the RANS and URANS mode calculates a near zero spanwise velocity at these locations (Viswanathan and Tafti, 2004).

While the spanwise flow in the rib vicinity is fairly well established by the fourth rib pair for both DES and LES, the secondary flow in the cross-section takes longer to develop. Fig. 7 shows the development of the secondary flow in the y–z cross-section of the channel by means of streamlines

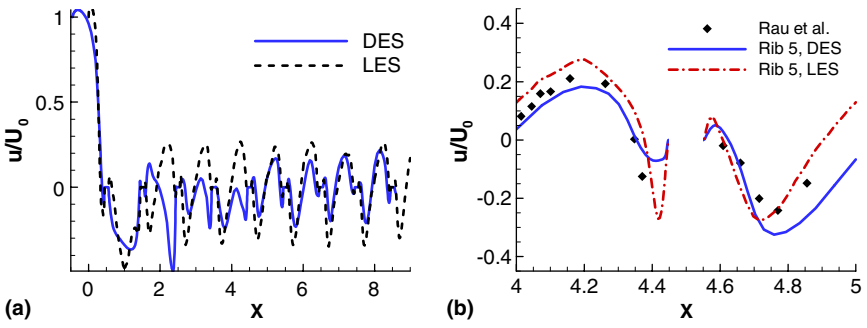

Fig. 5. (a) Development of the velocity profile at centerline of the $y/e = 0.25$ plane. (b) Velocity profile at $y/e = 0.1$ plane. Comparison with experiments and LES results at the 5th rib.

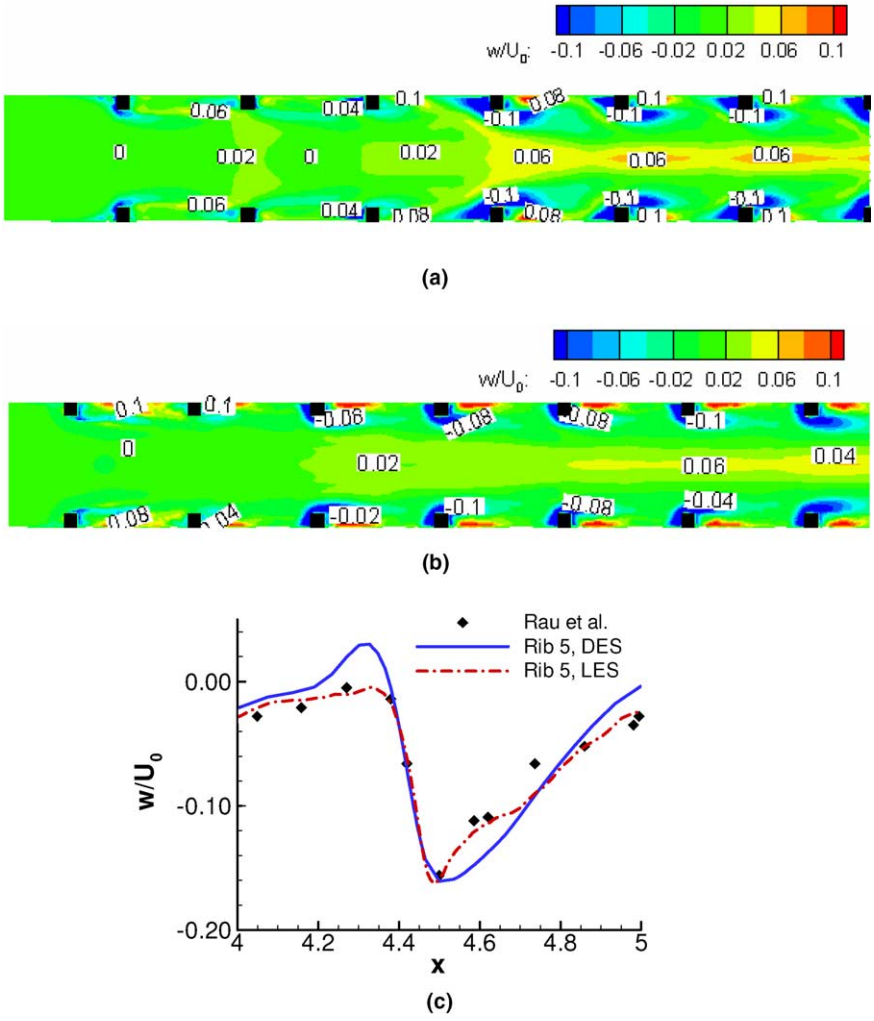

Fig. 6. Development of spanwise velocity in a plane $z/Dh = 0.05$ from the side wall as predicted by (a) DES (b) LES (Sewall et al., accepted for publication). (c) Comparison of the spanwise velocities near the 5th rib ($y/e = 1.5$, $z/Dh = 0.45$) with experiments (Rau et al., 1988) and LES (Sewall et al., accepted for publication).

that are defined using the v and the w-velocities. It is observed that immediately upstream of the first rib, the flow converges due to the presence of the ribs. This results in the secondary streamlines moving from the upper and the lower walls towards the center of the duct as shown in Fig. 7(a). As the flow progresses towards the 3rd rib, two rotating cells near each of the corners are observed on the side wall and on the ribbed wall. Between the fifth rib and the sixth rib the flow is similar to the flow observed in the fully developed case (Viswanathan and Tafti, 2004). An exception as shown in Fig. 7(c) is the extra rotating cell in each of the quadrants near the y-center line. This cell damps out downstream and the secondary flow observed after the 9th rib exactly resembles the flow in a fully developed case, as shown in Fig. 7(d).

7.1.4. Flow features in the 180° bend and second pass

Fig. 8 shows streamlines (defined using the u and the w-velocities) at three cross-stream locations $y = 0.5$, 0.3 and 0.15 for the flow entering and exiting the 180° bend as predicted by DES and LES.[3] As the flow approaches the bend, it accelerates at the inside of the bend and separates at the sharp edge of the bend. The separated region occupies the central 25–40% of the duct height and its shape and extent are predicted well by both methods. Additional separation zones are encountered in the outer corners of the bend. While LES predicts the existence of a strong recirculating region at the upstream corner throughout the height of the duct, DES predicts a smaller recirculating region, which does not quite sustain itself throughout the height of the duct. A small recirculation region downstream of the bend at the inner wall in the vicinity of the second rib is also predicted by both methods. Further, the flow is characterized

[3] The LES calculation was initiated 3 rib pitches upstream of the bend by using time-resolved inlet turbulent boundary conditions from another LES calculation of developing flow in a duct.

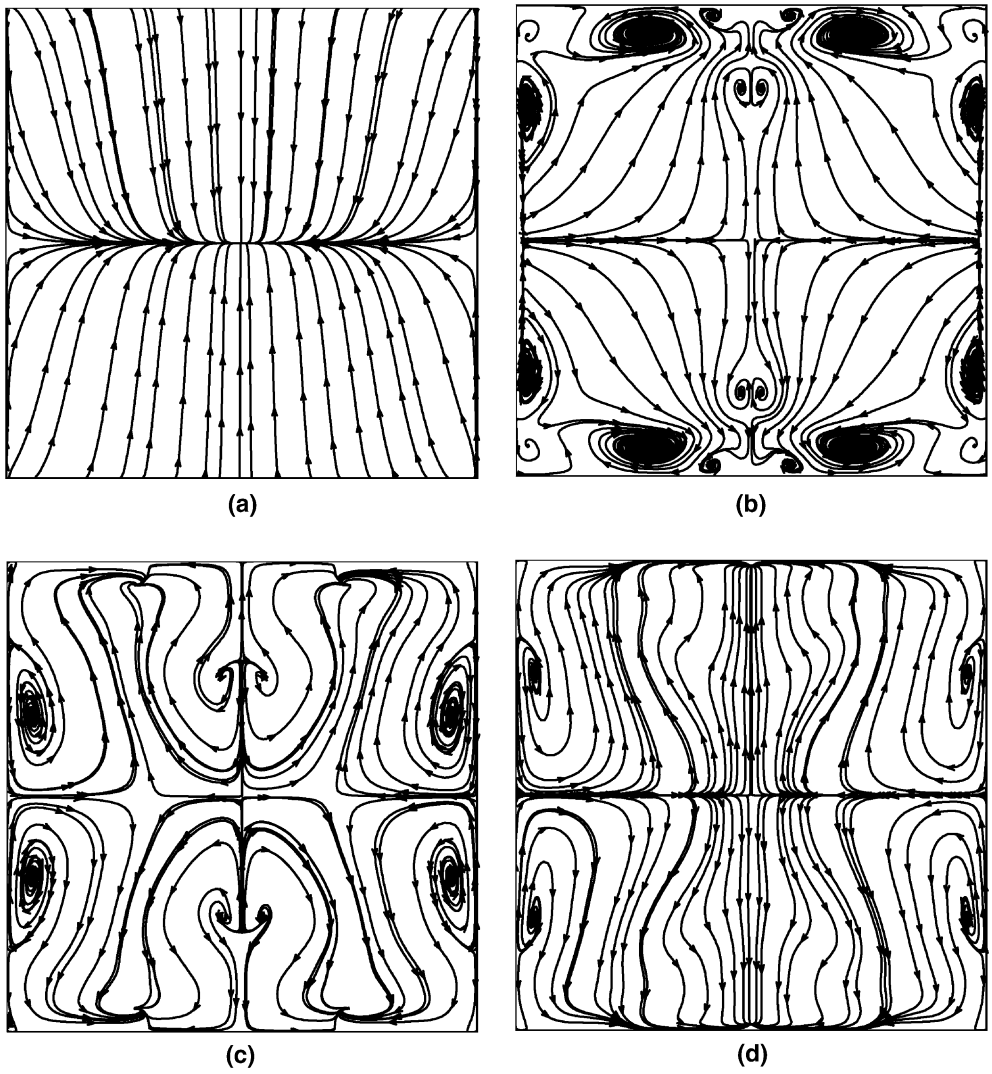

Fig. 7. Development of the secondary flow in the ribbed duct. (a) Upstream of the front rib, (b) between the 3rd and the 4th ribs, (c) between the 5th and the 6th ribs, (d) between the 9th and the 10th ribs. Maximum values of cross-sectional velocities (v, w) are about 0.10.

by impingement on the back wall and outer downstream wall of the duct which coincide with regions of high heat transfer.

Fig. 9 shows the comparison of the streamwise velocities at the center of the 180° bend (w-velocity in the bend) as predicted by DES and LES (Sewall and Tafti, 2005). The computed results are compared with LDV data from Sewall et al. (accepted for publication). At all y-locations, the velocity in the outer part of the bend ($x = 12.0$–12.5) is quite uniform at approximately 1.5 times the bulk velocity. However, at the inside of the bend, the streamwise velocity steadily decreases as y increases with a reversal in the flow direction occurring between $y = 0.27$ and 0.37. The profile at $y = 0.27$ shows a velocity of nearly zero, indicating that the recirculation zone occupies about 25% of the height of the duct. It is observed that in all the six locations DES predictions match well with experiments. Interestingly, DES comparisons are better than LES at these locations and could be a consequence of the inlet boundary conditions applied to the LES calculation upstream of the bend.

The variation of secondary cross-sectional flows in the vicinity of the 180° bend is shown in Fig. 10. In between the 10th and the 11th rib, the secondary flows are fully developed and small secondary cells are observed in each of the corner as shown in Fig. 10(a). As the flow crosses the 12th rib, it separates behind the rib. However, since the flow turns around the bend, the relative angle of the rib with respect to the flow is skewed. This results in a small recirculation zone downstream of the rib near the inner wall, as shown in Fig. 10(b). This recirculation develops into an L-shaped cell at the inner wall as the flow moves further into the bend. The secondary flow at the center of the 180° bend is characterized by Dean vortices impinging on the inner and outer walls which are responsible for high heat transfer at these walls. Further downstream (Fig. 10(d)) at the third rib in the second pass, the flow

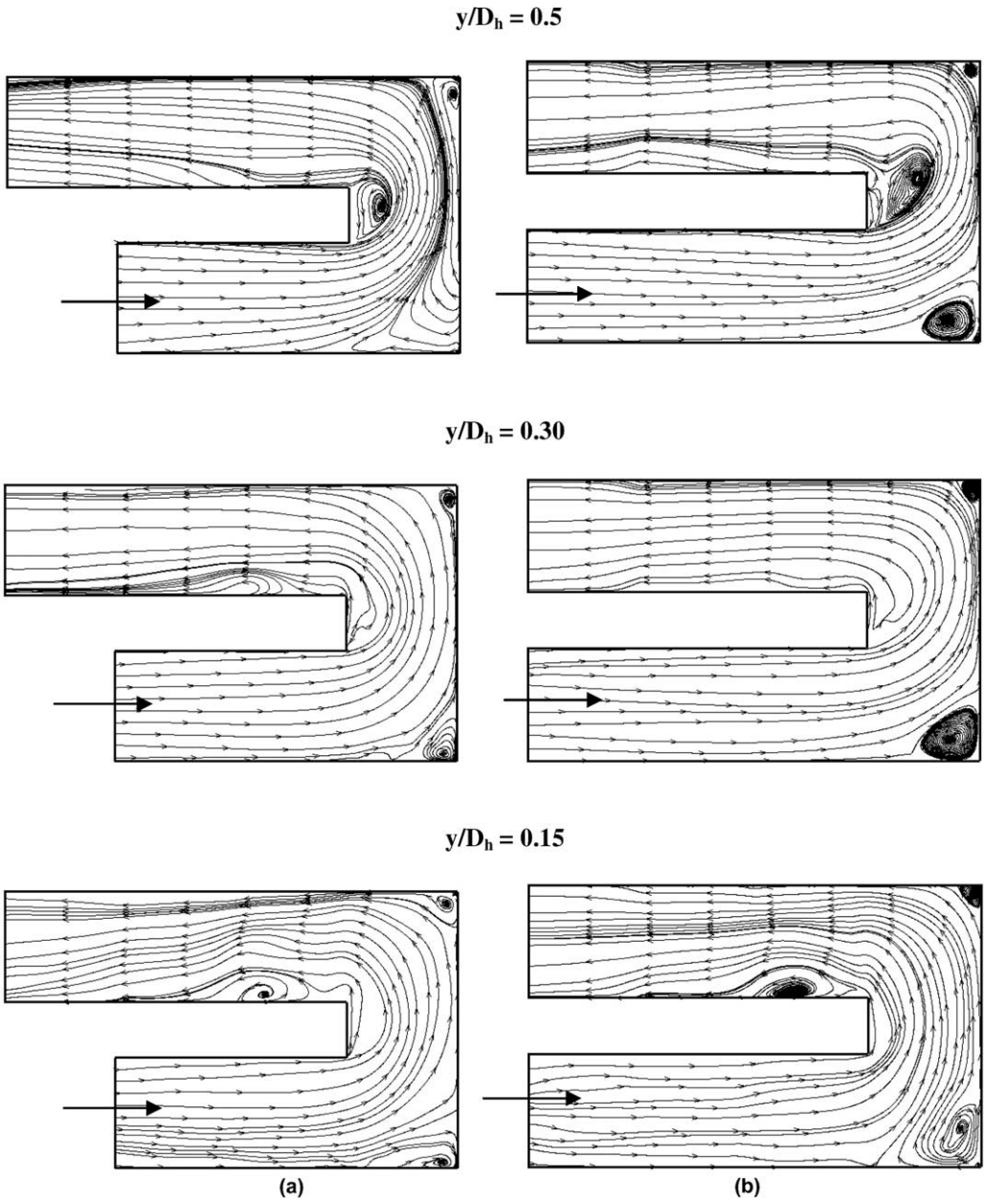

Fig. 8. Streamline distribution at three cross-stream locations of flow in the 180° bend: (a) DES and (b) LES.

from the inner wall towards the center of the channel is observed to be more dominant than the flow from the outer wall. Impingement is observed at the ribbed walls and is skewed towards the outer wall, which results in higher heat transfer at the ribbed wall closer to the outer wall. It is also observed that the secondary flow coming out of the bend is much stronger than that in the first pass with maximum cross-sectional velocities up to 40% of the mean streamwise velocity and persists far downstream in to the second leg till the 12th rib.

Fig. 11 shows the streamwise and the spanwise velocity contours at the center of the duct in the second pass. The maximum streamwise velocity in the second pass is skewed towards the outer wall, rather than at the center as observed in the first pass of the channel. A contour plot of the *w*-velocities shows movement of fluid from the inner wall towards the center of the duct. Though this feature is observed at the outer wall too, it is more prominent near the inner wall. This asymmetry is observed to persist till the last rib in the second pass of the channel.

7.1.5. Pitch averaged frictional losses

Frictional losses in ribbed ducts comprise of skin friction and form loss. Form losses make up 85–90% of the overall pressure drop which comprises the friction factor (Tafti, 2005). Fig. 12 shows the variation of the total friction factor and the contribution made by skin friction in the complete duct. Fig. 12(a) shows the comparison of

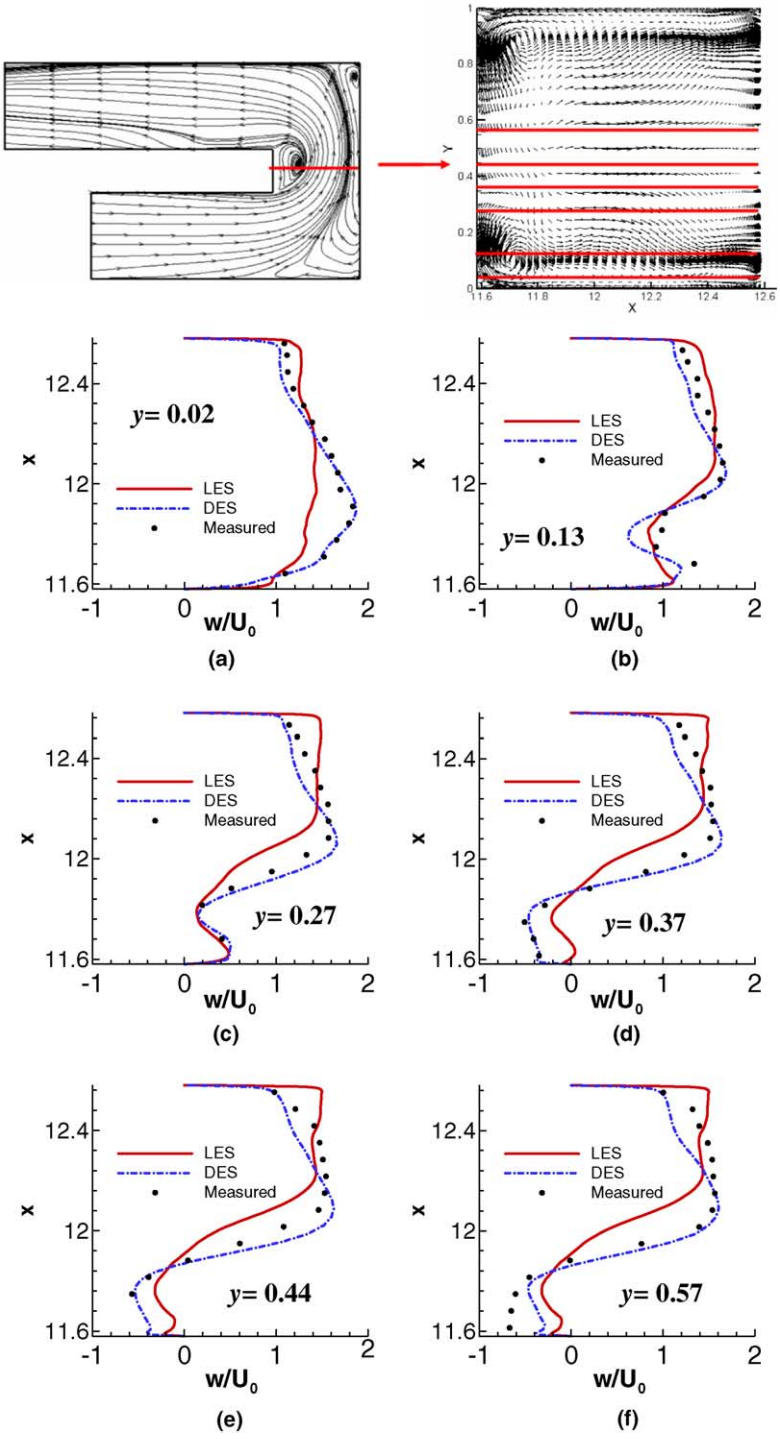

Fig. 9. Schematic diagram of the lines where the measurements have been presented (top). Comparison of the streamwise (w) velocities at the center of the 180° bend at different cross-stream locations.

the friction factor values obtained from DES with the LES computations (Sewall et al., accepted for publication; Sewall and Tafti, 2005). The LES data has been collected from two cases: stationary developing flow (Sewall et al., accepted for publication) for the first 9 ribs in the first pass, and LES computations in a 180° bend (Sewall and Tafti, 2005), for the 180° bend and two ribs upstream and downstream of the bend. In the DES computation the data is obtained by using the average pressure drop across one pitch ($f = -\Delta p/2\Delta l$) across a rib and the data is fitted to a spline. The skin friction coefficient in Fig. 12(b) is computed from the area averaged shear stresses on each of the walls—inner, outer and the ribbed walls.

As mentioned earlier, significant difference is observed in the entry region for the first three rib pairs where the mismatch between the LES and the DES computations is

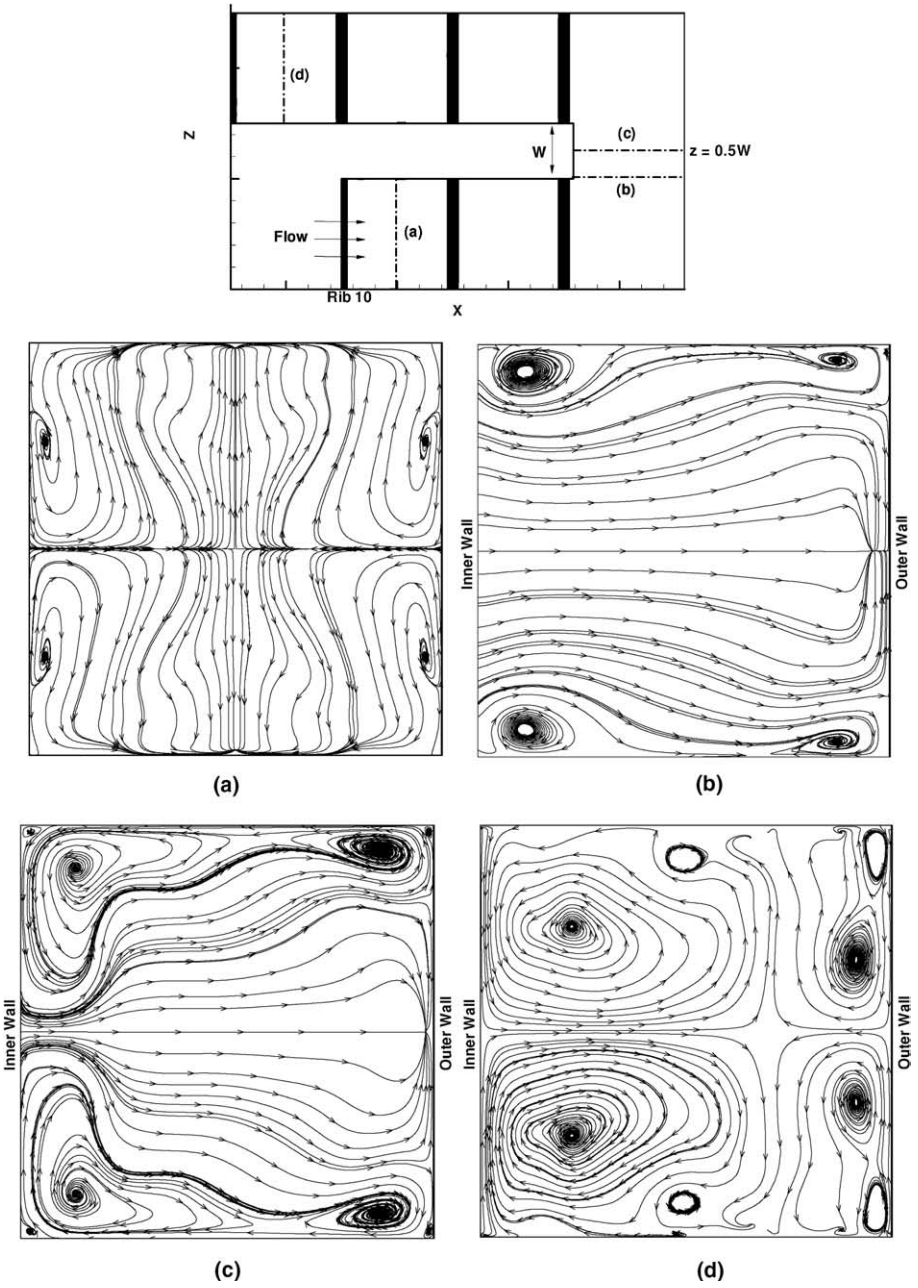

Fig. 10. Streamlines at the (a) developed flow at 10th rib; (b) 180° bend entrance, 12th rib; (c) $z/W = 0.5$; (d) between the 3rd and the 4th ribs in the second pass. Maximum values of cross-sectional velocities at locations (b) and (c) is of magnitude 0.2 and at location (d) of magnitude 0.4.

evident. DES does not accurately predict transition and the quick onset of turbulence. As a consequence, friction factor is under predicted. Good agreement is however observed after the 4th rib in the first pass of the channel. The average friction factor from the 4th rib to the 10th rib is observed to be around 8.15 times that in a smooth channel, which compares well with the LES value of 8.5. The shear induced due to the turning of the flow upstream of the 180° bend results in a higher friction factor in the region. The friction factor of 25.8 in this region is observed to be around three times that in a fully developed case. This value compares well with the LES value of 21. The calculated friction factor in the bend itself is about 28 as compared to the LES value of 20. Slight differences with the LES are observed since the LES computation was carried out assuming a fully developed turbulent flow two ribs upstream of the bend, while a complete channel is studied in this case. The flow encounters a large pressure drop as it turns the corner due to which a friction factor of about 40 is observed at the first rib section (block 14) immediately downstream of the bend. The corresponding LES value was about 37. In the subsequent block, pressure recovery results in a small negative friction coefficient. This is similar to the entry region where an initial drop in pressure is followed by pressure recovery.

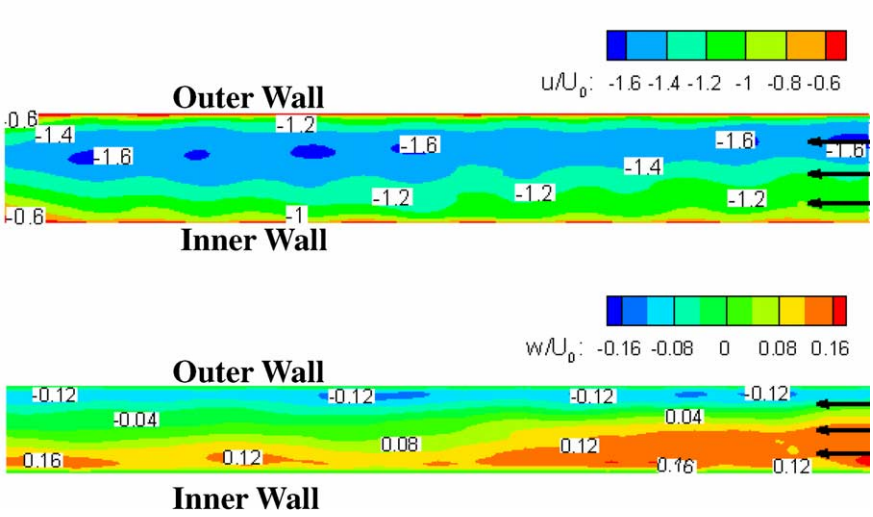

Fig. 11. Streamwise and spanwise velocity components in the second pass of the channel. Positive w-velocities indicate flow moving away from the inner wall.

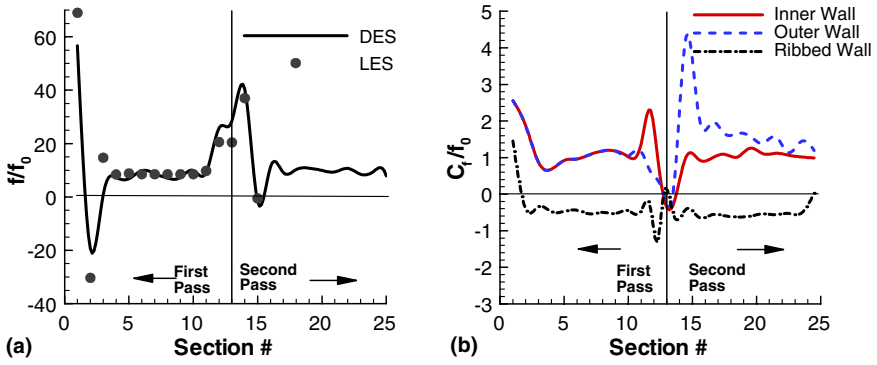

Fig. 12. Variation of (a) friction factor and (b) co-efficient of friction at the three walls in the two-pass channel.

As the flow settles down in the second pass, the average friction factor in the second pass of the duct is observed to be close to 9.5 as predicted by the DES computations.

Fig. 12(b) shows the skin-friction coefficient at the inner wall, outer wall and the ribbed wall. Negative friction is observed on the ribbed wall as a result of the recirculation regions occupying a major part of the ribbed wall. In the 180° bend a small positive friction factor is observed. The trend in the second pass of the channel with regards to the ribbed wall friction is the same as the first pass of the channel. The friction at the inner and outer walls is the same in the first pass of the channel. However as the flow approaches the 180° bend the skin friction increases substantially at the inner wall because of increased shear followed by a drop in the bend due to the flow separation at the inner wall. In the second pass of the channel it is observed that the skin-friction at the outer wall is much larger than the friction at the inner wall. This is due to the higher velocities observed at the outer wall as shown in Fig. 9. The difference between the two decreases as the flow moves downstream. However it is observed that differences still exist as far downstream as the 12th rib.

7.2. Heat transfer augmentation

7.2.1. Heat transfer in the developing region

The heat transfer development in the first pass of the channel is shown in Fig. 13 at the side wall just upstream of the rib in the region of secondary flow impingement and at the center of the ribbed wall. At rib 3, the secondary flow impingement on the side wall is not yet fully established and this is reflected in the lower augmentation ratios at $y = 0.1$ in Fig. 13(a). The side wall augmentation develops till the fifth rib, after which the distribution exhibits a quasi-periodic state. Similar observations can be made at the ribbed wall.

Fig. 13(c) shows the comparisons of the heat transfer augmentation at the side walls of the first pass immediately upstream ($0.05D_h$ upstream) of the 6th rib with the LES and experiments (Rau et al., 1988). The heat transfer augmentation shows good agreement with both the experiments and the LES results. The heat transfer is highest in the region of secondary flow impingement and decreases towards the center of the duct. Both LES and DES overpredict the peak augmentation. While LES predicts low

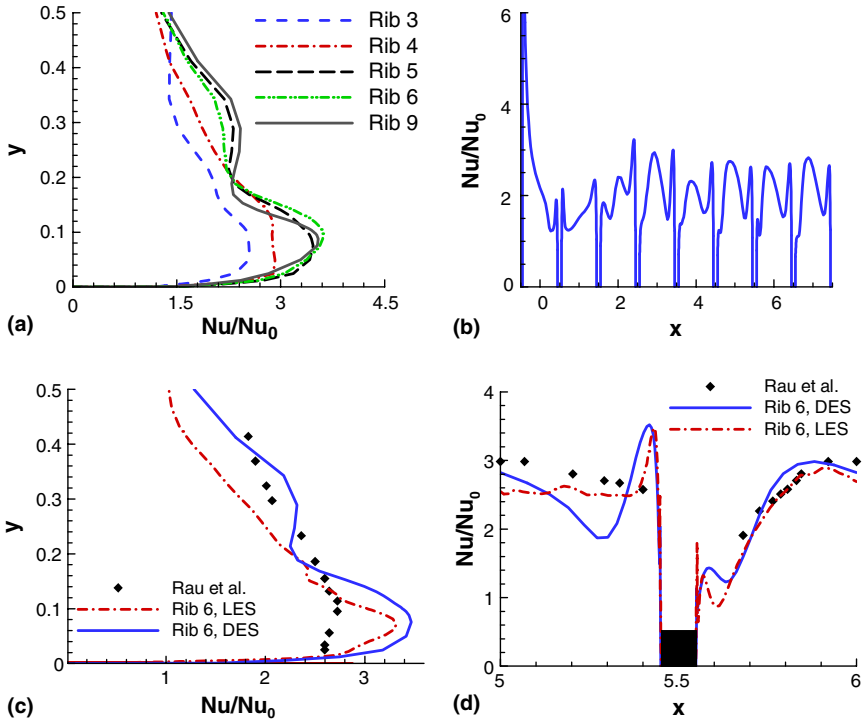

Fig. 13. Heat transfer development at the (a) side wall ($x = 0.05D_h$ upstream of the rib), (b) ribbed wall ($z = 0.5$), (c) comparisons upstream of the rib ($x = 0.05D_h$ upstream) on the smooth wall with experiments (Rau et al., 1988) and LES. (d) Comparison of the augmentation ratios at the *center of* the ribbed wall.

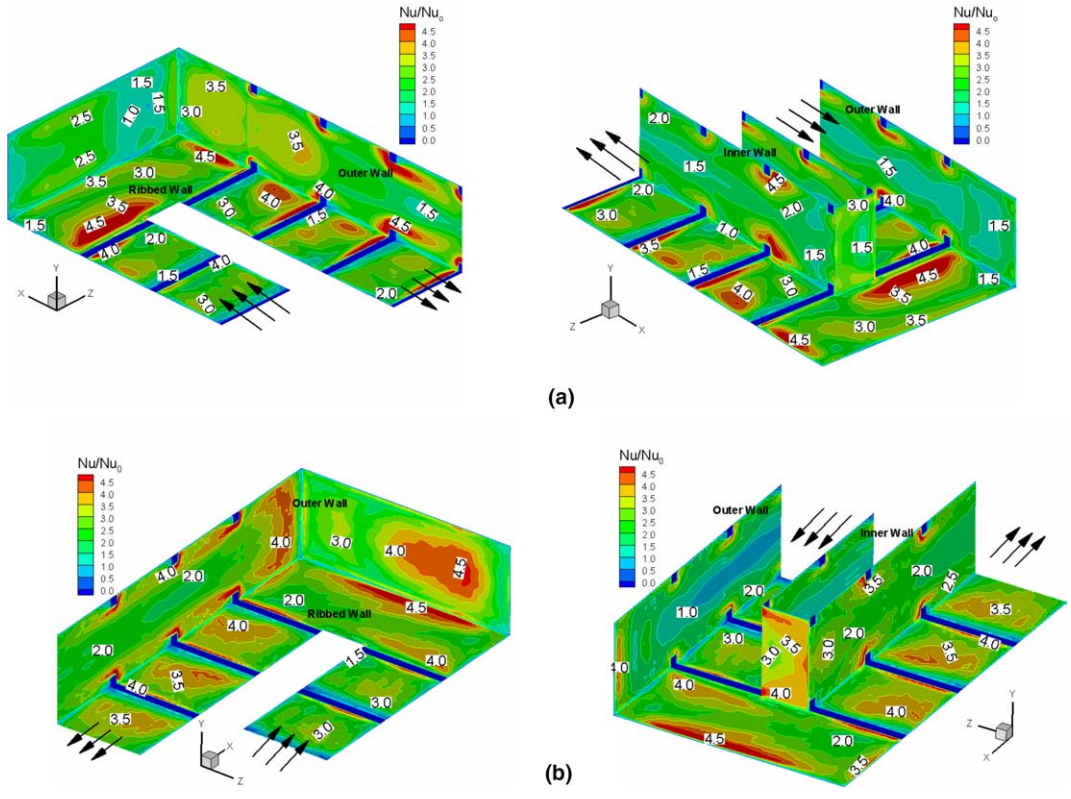

Fig. 14. Augmentation ratios in the vicinity of the 180° bend: (a) DES and (b) LES (Sewall et al., accepted for publication).

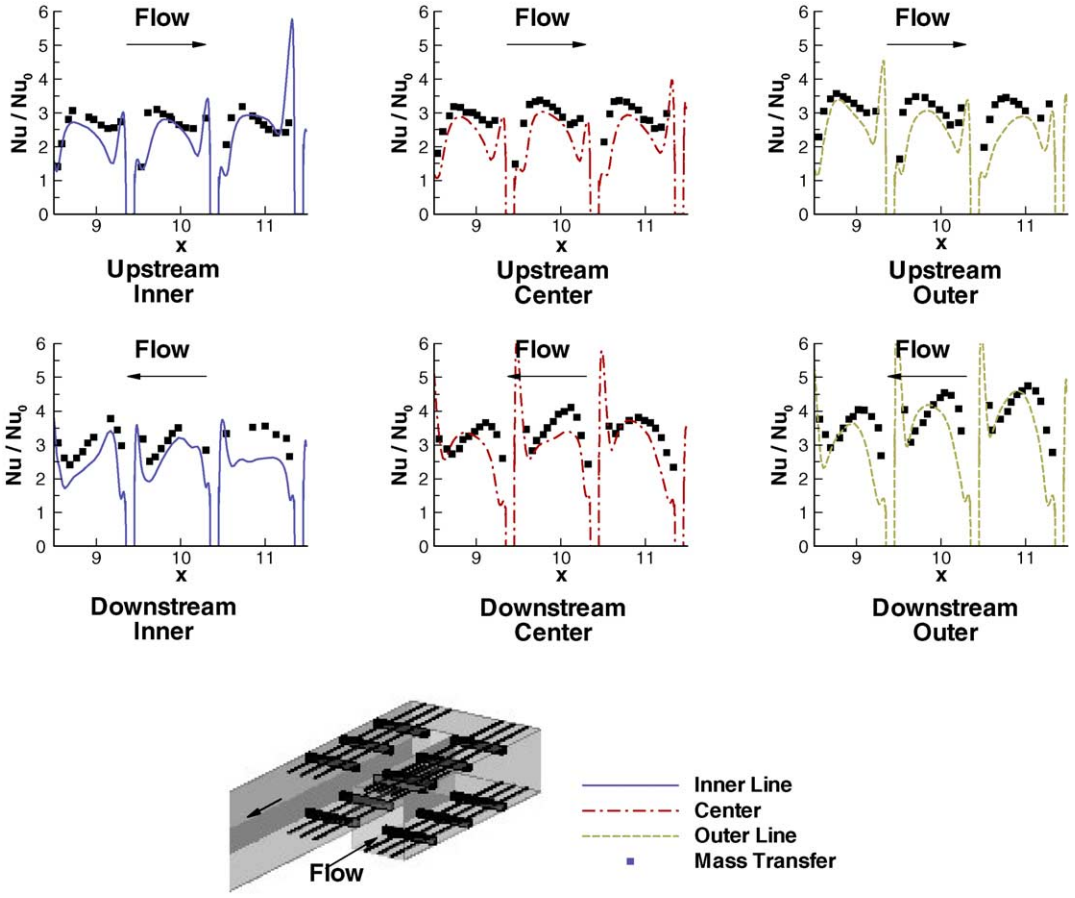

Fig. 15. Comparison of the augmentation ratios predicted by DES upstream and downstream of the bend with experiments (Han et al., 1988).

augmentation ratios at the center of the duct, DES predictions are in much better agreement with the experiments. The underprediction by LES is attributed to a coarse mesh at the center, whereas the use of RANS at the center with DES compensates for this and gives a better prediction.

The heat transfer at the ribbed wall is shown in Fig. 13(d). In between the two ribs (after reattachment of the flow) both DES and LES under predict the heat transfer, the degree of underprediction more so for DES than LES. However both methods show good agreement with experimental data, accurately predicting the high heat transfer ($Nu/Nu_0 = 3.5$) immediately upstream of the rib, which is a result of highly unsteady vortical flow in this region. These secondary vortices entrain fluid from the main stream, thereby transferring heat from the hot walls to the core of the channel. A region of low heat transfer immediately downstream of the rib is also predicted, which is caused by the presence of secondary trapped eddies. Further downstream in the primary recirculation region, the heat transfer from the walls is gradually enhanced and reaches a maximum at around $3.5e$ downstream of the rib. The point of maximum heat transfer is slightly upstream of the reattachment, where the surface shear is a maximum. The general trends indicate that DES predictions are accurate in the recirculating region, but tend to underpredict after reattachment. DES also tends to predict an exaggerated region of high heat transfer in front of the rib.

7.2.2. Heat transfer in the 180° bend

The heat transfer predictions at the 180° bend are shown in Fig. 14. On approaching the 180° bend the flow becomes asymmetric due to which the heat transfer is no longer symmetric in the z-direction. Immediately upstream of the 180° bend, where the flow starts to turn, higher heat transfer are observed at the inner wall. Regions of high heat transfer, with augmentation up to 4.5, are observed on the ribbed wall, as the flow enters the 180° bend after passing over the final rib. At this location the relative angle of the flow with respect to the last rib induces flow similar to a duct with skewed ribs. Hot spots, where the heat transfer is low are observed at the corner of the 180° bend due to the presence of the recirculation zones. High heat transfer ($Nu/Nu_0 = 2.5$–3.0) are also observed at the outer and inner walls of the 180° bend where flow impingement by the action of Dean vortices results in local cooling. The augmentation at the junction of the ribbed wall with the outer wall of the bend is also a result of flow impingement and transport by the action of the Dean vortices in the cross-section. The surface distribution pattern predicted

by DES compares very well with LES; however, the augmentation ratio predicted by LES is generally higher.

The presence of the bend affects the flow and therefore the heat transfer downstream of the bend. Immediately downstream of the bend, in the first and the second rib sections of the second pass, high heat transfer is observed (3.5–4.5) at the outer wall due to the effect of flow impingement. At the ribbed wall higher heat transfer is observed closer to the outer wall due to the asymmetric flow in the region and the presence of the secondary flow in the cross-section. These trends are also consistent with the LES results.

Fig. 15 shows the comparison of the heat transfer at the ribbed wall upstream and downstream of the 180° bend along three lines—near the inner wall, along the center and near the outer wall. The predictions are compared to the experiments of Han et al. (1988). The experiments were performed in a geometry similar to the one used in this study with slight differences ($e/D_h = 0.094$, $P/e = 10$ at a Reynolds number of 30,000). One difference between the two studies is the width of the dividing wall between the upstream and downstream ducts, which is $\frac{1}{4}D_h$ in the experiments and $\frac{1}{2}D_h$ in the calculations. This parameter has an important effect on the flow and heat transfer characteristics, as was shown in a smooth wall 180° bend study by Liou et al. (1999). In spite of the difference, the DES predictions compare reasonably well with the experiments. While the heat transfer was observed to be near symmetric in the developing region of the first pass, a significant difference in the heat transfer values can be observed as the flow approaches the bend. The skewness prevails in the second pass of the channel.

The general heat transfer downstream of the 180° bend is higher than the heat transfer upstream. Similar observations were also made in earlier studies by Ekkad and Han (1997), where the heat transfer profiles at the center of the ribbed wall showed the effect of the bend on the heat transfer in the second pass.

7.2.3. Heat transfer in the second pass

The heat transfer in the second pass is a function of the distance from the 180° bend. Closer to the 180° bend the flow is highly asymmetric. The flow tries to regain symmetry gradually but it is observed that even after 12 ribs the asymmetry prevails. Fig. 16 shows the heat transfer augmentation at the ribbed wall and the outer and the inner walls. Due to the asymmetry in the flow, higher heat transfer is observed at the outer wall. It is also observed that the

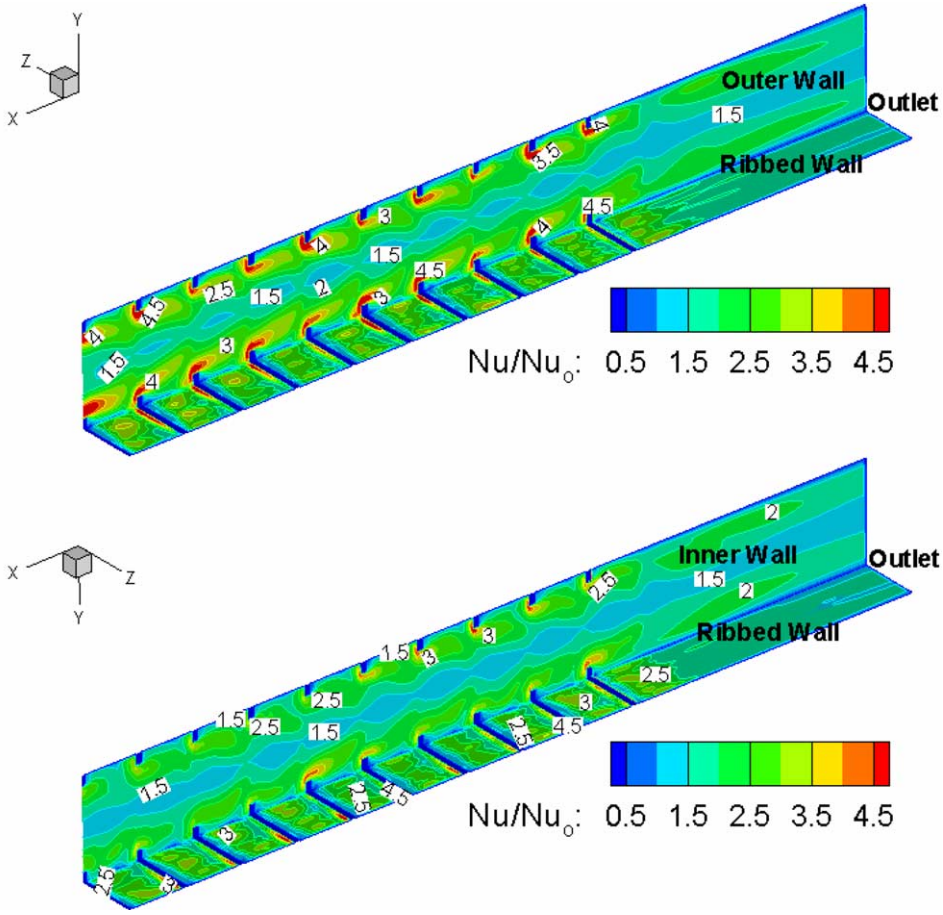

Fig. 16. Augmentation ratios at the ribbed, inner and the outer walls in the second pass of the internal cooling duct.

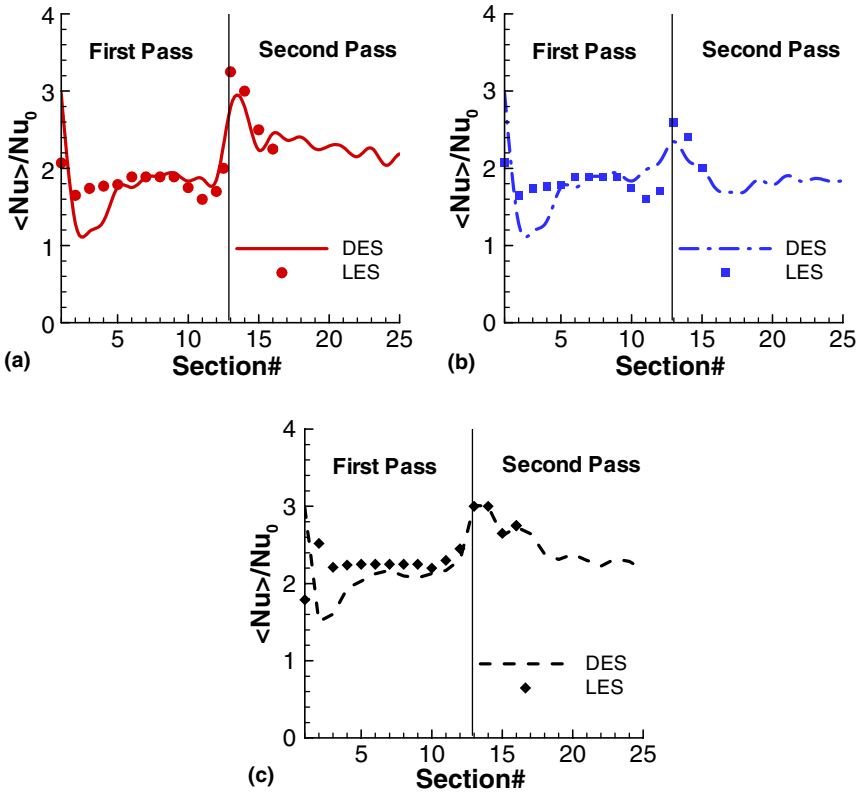

Fig. 17. Overall heat transfer augmentation at the walls: (a) outer wall, (b) inner wall and (c) ribbed wall.

heat transfer levels at both the inner and the outer walls are greater than the heat transfer augmentation observed in the first pass of the channel.

7.2.4. Pitch averaged heat transfer augmentation

Fig. 17 shows the comparison of the pitch averaged heat transfer predicted by the DES with LES computations (Sewall et al., accepted for publication; Sewall and Tafti, 2005) at the ribbed and the side walls. A discrepancy in the predictions is observed for the first 4 ribs in the developing region of the duct. As explained earlier this is due to the inability of DES to predict transition accurately. However after the flow is (hydrodynamically and thermally) developed the predictions by DES are consistent with LES predictions. Heat transfer increases in the vicinity of the 180° bend at all the walls. The DES predictions in the vicinity of the 180° bend also are consistent with the LES results, though the values are slightly over-predicted at the inner wall. In the second pass of the duct, the heat transfer at all the walls is higher than the first pass, due to the increase in turbulence and stronger secondary flows. Experiments by Liou et al. (2002) also showed a similar increase in overall heat transfer in the second pass of the duct. The overall heat transfer at the outer wall of the second pass is observed to be higher than the heat transfer at the inner wall, which is consistent with the trends observed by Wagner et al. (1992) in their experiments on ducts with normal ribs.

8. Conclusions

The capability of DES in predicting the flow and heat transfer in a complete two pass channel has been evaluated. The LES computation in the developing region of the duct used around 8.85×10^6 cells (Sewall et al., accepted for publication) and 8.4×10^6 cells were used in the LES computation in a 180° bend (Sewall and Tafti, 2005). A DES computation of the complete two pass channel was carried out by discretizing the whole domain in to 7.7×10^6 cells. DES overcomes the challenges faced by common RANS models in predicting separation regions behind the rib by switching to an LES formulation in this region. The flow and heat transfer in the developed region of the duct compares well with the LES computations by Tafti (2005), Sewall et al. (accepted for publication) and experiments by Rau et al. (1988). The flow and heat transfer in the 180° bend are also consistent with the LES results in the bend by Sewall and Tafti (2005) and experimental results by Han et al. (1988) and Sewall and Tafti (2004b).

DES does not predict shear layer transition with accuracy and as a result predicts a greater development length than LES. While LES predicts a near-fully developed state after the third rib pair from the entrance, DES does not exhibit a similar state till the fifth rib pair. However, once this state is attained, DES predictions compare well with LES and experiments. Secondary flows, separation and reattachment match the fully developed flow conditions.

The flow in the inter-rib spacing is dominated by vortex enhanced heat transfer in front of the rib, in the reattachment region behind the rib and at the junction of the rib with the smooth walls. The latter manifests itself as a mean lateral movement of fluid impinging on the smooth wall (secondary flow). The flow in the 180° bend is characterized by impingement at the inner and the outer wall of the bend and at the outer wall downstream of the bend. This results in high levels of heat transfer at these walls. Additionally secondary Dean vortices have a large impact on the heat transfer. The effect of the 180° bend is felt upstream of the bend in the vicinity of the 11th and the 12th ribs, where the heat transfer is higher at the inner wall. Downstream of the 180° bend the heat transfer is higher at the outer wall. The flow in the second pass of the channel is asymmetric, due to the presence of the 180° bend upstream. The secondary flows are much more prominent in the second pass, and as a result, the heat transfer is higher compared to the first pass of the duct.

Pitch averaged friction coefficient augmentation ranges from 9 in the fully developed region of the first pass to values as high as 40 coming out of the 180° bend whereas heat transfer augmentation ranges from 2.3 on the ribbed wall in the fully developed region to 3.0 in the bend.

It is concluded that in spite of shortcomings in predicting transition correctly at the entrance to the duct, DES predicts flow and heat transfer with good accuracy in a flow which is dominated by separation and reattachment of shear layers, unsteady vortex induced secondary motions, and strong streamline curvature. In all aspects it reproduces the correct physics and shows good quantitative comparisons with LES and experiments while reducing the computational complexity by nearly an order of magnitude. The gains are expected to be much more at higher Reynolds numbers.

References

Abdel-Wahab, S., Tafti, D.K., 2004a. Large eddy simulations of flow and heat transfer in a 90° ribbed duct with rotation—effect of coriolis and centrifugal buoyancy forces. In: GT2004-53799, ASME Turbo Expo 2004, Vienna, Austria. J. Turbomach. 126 (4), 627–636.

Abdel-Wahab, S., Tafti, D.K., 2004b. Large eddy simulation of flow and heat transfer in a staggered 45° ribbed duct. GT2004-53800, ASME Turbo Expo 2004, Vienna, Austria.

Amano, R.S., Goel, P., 1995. Computation of turbulent flow beyond backward steps using Reynolds stress closure. AIAA J 23, 1356.

Driver, D., Seegmiller, H.L., 1985. Features of reattaching turbulent shear layer in divergent channel flow. AIAA J. 23, 162–171.

Ekkad, S.V., Han, J.C., 1997. Detailed heat transfer distributions in tow-pass square channels with rib turbulators. Int. J. Heat Mass Transfer 40 (11), 2525–2537.

Forsythe, J.R., Squires, K.D., Wurtzler, K.E., Spalart, P.R., 2002. Detached–eddy simulation of fighter aircraft at high alpha. AIAA Paper 2002-0591.

Han, J.C., Chandra, P.R., Lau, S.C., 1988. Local heat/mass transfer distributions around sharp 180 deg turns in two-pass smooth and rib-roughened channels. J. Heat Transfer 110 (February), 91–98.

Iacovides, H., 1998. Computation of flow and heat transfer through rotating ribbed passages. Int. J. Heat Fluid Flow 19, 393–400.

Iacovides, H., Raisee, M., 1999. Recent progress in the computation of flow and heat transfer in internal cooling passages of turbine blades. Int. J. Heat Fluid Flow 20, 320–328.

Incropera, F.P., Dewitt, D.P., 2002. Fundamentals of Heat and Mass Transfer, fifth ed. John Wiley and Sons, New York.

Jia, R., Saidi, A., Sunden, B., 2002. Heat transfer enhancements in square ducts with V-shaped ribs of various angles. In: GT 2002-30209, Proc. ASME Turbo Expo.

Johnson, B.V., Wagner, J.H., Steuber, G.D., Yeh, F.C., 1994. Heat transfer in rotating serpentine passages with selected model orientations for smooth or skewed trip walls. J. Turbomach. 116 (Oct.), 738–744.

Kapadia, S., Roy, S., Wurtlzer, K., 2003. Detached eddy simulation over a reference Ahmed car model. AIAA 2003-0857.

Liou, T.-M., Hwang, J.J., Chen, S.H., 1992. Turbulent transport phenomena in a channel with periodic rib turbulators. J. Thermophys. Heat Transfer 6 (3), 513–521.

Liou, T.-M., Tzeng, Y.-Y., Chen, C.-C., 1999. Fluid flow in a 180 deg sharp turning duct with different divider thicknesses. ASME J. Turbomach. 121, 569–576.

Liou, T.-M., Chen, M.-Y., Tsai, M.-H., 2002. Fluid flow and heat transfer in a rotating two-pass square duct with in-line 90-degree ribs. ASME J. Turbomach. 125, 260–268.

Menter, F.R., 1992. Improved two-equation k–ω turbulence models for aerodynamic flows. NASA Technical Memorandum 103975, October 1992.

Menter, F.R., 1993. Zonal Two Equation k–ω Turbulence Models for Aerodynamic Flows, AIAA Paper 93-2906.

Murata, A., Mochizuki, S., 2001. Comparison between laminar and turbulent heat transfer in stationary square ducts with transverse or angled rib turbulators. Int. J. Heat Mass Transfer 44, 1127–1141.

Ooi, A., Iaccarino, G., Durbin, P.A., Behnia, M., 2002. Reynolds averaged simulation of flow and heat transfer in ribbed ducts. Int. J. Heat Fluid Flow 23, 750–757.

Patrick, W., Tafti, D.K., 2004. Computations of flow structure and heat transfer in a dimpled channel at low to moderate Reynolds number. In: HT-FED2004-56171, 2004 ASME Heat Transfer/Fluids Engineering Summer Conference, July 11–15, Charlotte.

Prakash, C., Zerkle, R., 1995. Prediction of turbulent flow and heat transfer in a ribbed rectangular duct with and without rotation. ASME J. Turbomach. 117 (April), 255–264.

Rau, G., Cakan, M., Moeller, D., Arts, T., 1988. The effect of periodic ribs on local aerodynamic and heat transfer performance of a straight cooling channel. ASME J. Turbomach. 120, 368–375.

Rigby, D.L., 1998. Prediction of heat and mass transfer in a rotating ribbed coolant passage with a 180 degree turn. In: 98-GT-329, International Gas Turbine and Aeroengine Congress and Exhibition, Stockholm, Sweden, June 2–5, 1998.

Saidi, A., Sunden, B., 2001. On prediction of thermal-hydraulic characteristics of square-sectioned ribbed cooling ducts. ASME J. Turbomach. 123, 2001.

Sewall, E.A., Tafti, D.K., 2004a. Large eddy simulation of the developing region of a stationary ribbed internal turbine blade cooling channel. In: GT2004-53832, ASME Turbo Expo 2004, Vienna, Austria.

Sewall, E.A., Tafti, D.K., 2004b. Large eddy simulations of the developing region of a rotating ribbed internal turbine blade cooling channel. In: GT2004-53833, ASME Turbo Expo 2004, Vienna, Austria.

Sewall, E.A., Tafti, D.K., 2005. Large Eddy Simulation of Flow and Heat Transfer in the 180° bend Region of a Stationary Ribbed Gas Turbine internal Cooling Duct. In: GT 2005-68518, ASME Turbo Expo 2005, June 6–9, 2005, Reno-Tahoe, Nevada, USA.

Sewall, E.A., Tafti, D.K., Graham, A., Thole, K.A., accepted for publication. Experimental validation of large eddy simulation of flow and heat transfer in a stationary ribbed duct. Int. J. Heat Fluid Flow.

Spalart, P.R., Jou, W.H., Streletes, M., Allmaras, S.R., 1997. Comments on the feasibility of LES for wings and a hybrid RANS/LES approach. In: First AFSOR Int. Conf. on DNS/LES, Aug 4–8, 1997. In: Liu, C., Liu, Z. (Eds.), Advances in DNS/LES. Greyden Press, Columbus, OH.

Squires, K.D., Forsythe, J.R., Morton, S.A., Blake, D.C., Serrano, M., Wurtzler, K.E., Strang, W.Z., Tomaro, R.F., Spalart, P.R., 2002. Analysis of full aircraft with massive separation using detached–eddy simulation. In: Proc. of the High Performance Computing Modernization Program 2002 Users Group Conf., Austin, Texas.

Strelets, M., 2001. Detached eddy simulation of massively separated flows. AIAA 2001-0879.

Tafti, D.K., 2001. GenIDLEST—A scalable parallel computational tool for simulating complex turbulent flows. In: Proc. ASME Fluids Engineering Division, FED, vol. 256, ASME-IMECE, New York.

Tafti, D.K., 2005. Evaluating the role of subgrid stress modelling in a ribbed duct for the internal cooling of turbine blades. Int. J Heat Fluid Flow 26 (1), 92–104.

Viswanathan, A.K., Tafti, D.K., 2004. Detached eddy simulation of turbulent flow and heat transfer in a duct, HT-FED2004-56152, 2004 ASME Heat Transfer/Fluids Engineering Summer Conference, July 11–15, Charlotte. J. Fluids Engineering, 127(5), September 2005, in press.

Viswanathan, A.K., Tafti, D.K., 2005. Detached eddy simulation of flow and heat transfer in a stationary internal cooling duct with skewed ribs. In: GT 2005-68118, ASME Turbo Expo 2005, June 6–9, 2005, Reno-Tahoe, Nevada, USA.

Viswanathan, A.K., Tafti, D.K., Abdel-Wahab, S., 2005. Large eddy simulation of flow and heat transfer in an internal cooling duct with high-blockage 45° staggered ribs. In: GT 2005-68086, ASME Turbo Expo 2005, June 6–9, 2005, Reno-Tahoe, Nevada, USA.

Wagner, J.H., Johnson, B.V., Graziani, R.A., Yeh, F.C., 1992. Heat transfer in rotating serpentine passages with trips normal to the flow. ASME J. Turbomach. 114, 847–857.

Watanabe, K., Takahashi, T., 2002. LES simulation and experimental measurement of fully developed ribbed channel flow and heat transfer. In: Proc. of the ASME Turbo Expo, Amsterdam, The Netherlands, June 2002.

Wilcox, D.C., 1988. Reassessment of the scale-determining equation for advanced turbulence models. AIAA J. 26 (11), 1299–1310.